CHAPTER NINETEEN

Using Anomalous Small Angle X-Ray Scattering to Probe the Ion Atmosphere Around Nucleic Acids

Suzette A. Pabit,* Kenneth D. Finkelstein,† *and* Lois Pollack*

Contents

Abstract

Anomalous small angle X-ray scattering (ASAXS) exploits contrast variation methods to highlight the scattering from one elemental component in a multi-element sample, such as one ion species in an ion–DNA system. The ASAXS

* School of Applied and Engineering Physics, Cornell University, Ithaca, New York, USA
† Cornell High Energy Synchrotron Source, Cornell University, Ithaca, New York, USA

Methods in Enzymology, Volume 469
ISSN 0076-6879, DOI: 10.1016/S0076-6879(09)69019-4

method has been applied to measure ions condensed around short nucleic acid duplexes. This chapter, which briefly describes the origin of the ASAXS signal, focuses on the experimental methods required to carry out these measurements and the interpretation of the anomalous signals.

1. Introduction

The high negative charge of DNA and RNA backbones is intimately linked to the structure and function of these macromolecules. To achieve electrical neutrality, this substantial charge is compensated by positively charged atoms/molecules, such as proteins, polyamines, or ions (Bloomfield *et al.*, 2000). For many RNAs, counterions provide sufficient screening to overcome repulsive forces; large RNAs fold to biologically functional structures following the addition of millimolar quantities of divalent ions to low ionic strength solution. Clearly, ion association to nucleic acids is important in facilitating biologically relevant interactions.

The importance of quantifying ion–nucleic interactions has long been recognized; numerous techniques have been applied to detect ions associated to (condensed around) nucleic acid strands. Past studies have monitored changing NMR relaxation rates for cations condensed around DNA (Anderson and Record, 1990). A second method detects associated counterions by monitoring energy transfer between luminescent lanthanide ions, which depends on the collision frequencies of condensed counterions (Wensel *et al.*, 1986). Ion-sensitive dyes provide precise calibration of free ion concentrations; ion binding can alter interaction with these indicators (Grilley *et al.*, 2009). Finally, inductively coupled plasma-atomic emission spectroscopy (ICP-AES or AES) (Bai *et al.*, 2007; Plum and Bloomfield, 1988) has been applied to determine the elemental composition of carefully buffer-exchanged samples containing DNA relative to a control sample which does not contain DNA. Differences in ion population in these two samples report the number of excess counterions or excluded coions due to the presence of the nucleic acid. The subject of this chapter is a technique that provides information about the spatial distribution of ions associated to DNA or RNA: anomalous SAXS (or ASAXS). These measurements enable direct comparison with theoretical predictions of ion spatial distribution. To date, much experimental effort has focused on measuring ions associated to short strands of DNA, due to the enhanced robustness (and reduced expense) of DNA relative to RNA. ASAXS results confirm the predicted dependence of ion spatial distribution on ion valence and competition. Most recently, ASAXS studies of ion–RNA systems illustrate key differences between ion association to RNA as opposed to DNA, highlighting the importance of helix topology.

2. Background: SAXS and ASAXS

2.1. Small angle X-ray scattering

We begin with a brief discussion of small angle X-ray scattering (SAXS). This valuable experimental technique provides information about the size, shape, compactness, and molecular weight of molecules in solution when their characteristic size is larger than the wavelength (λ) of the X-rays used, typically 1 Å (Doniach, 2001; Svergun and Koch, 2003). Thus, it is an ideal probe of nucleic acid conformation. SAXS experiments on macromolecules are typically conducted in solution, where molecules can freely change conformation; however, the orientation of molecules relative to the incident beam is unconstrained, so the SAXS signal reports a spherical average of molecular orientations. Some of the most recent analysis methods are discussed in Chapter 11.

Small angle scattering from RNA or DNA arises from phase differences between X-rays scattered from electrons at different locations within the macromolecule. The intensity of the scattered radiation is largest along the direction of the incident beam, and decreases as the scattering angle, 2θ, increases. The angular dependence of the scattered X-rays reflects the size and shape of the sample; at a given scattering angle the measured intensity relative to the maximum value at $2\theta = 0$ is smaller for larger objects, due to the greater path length (hence phase) difference of X-rays scattered from widely separated sources (Glatter, 1982). Thus, the angular dependence of the scattered radiation reflects the spatial distribution of electrons inside the sample, in this case the macromolecule. Figure 19.1 illustrates the geometry of a typical scattering experiment.

The strength of the scattering signal arises from the difference in electron density (or contrast) of the macromolecule relative to the background solvent. The measured intensity $I(2\theta)$ is directly proportional to the product of the molecular concentration and the square of the electron density difference between macromolecule and solvent (Svergun and Koch, 2003) at the corresponding length scale. When the scattering is from DNA or RNA, an additional component must be considered: the high-density cloud of counterions closely associated to the nucleic acid strand (Manning, 1969). For these systems, scattering arises from the excess electron density (contrast) of both the nucleic acid and the counterions relative to the uniform solvent background.

2.2. Anomalous SAXS provides measurements of ion distributions

Anomalous SAXS (ASAXS) takes advantage of contrast variation methods to highlight the small angle scattering signal from a single elemental component correlated with a larger system (Stuhrmann, 1981), for example, one

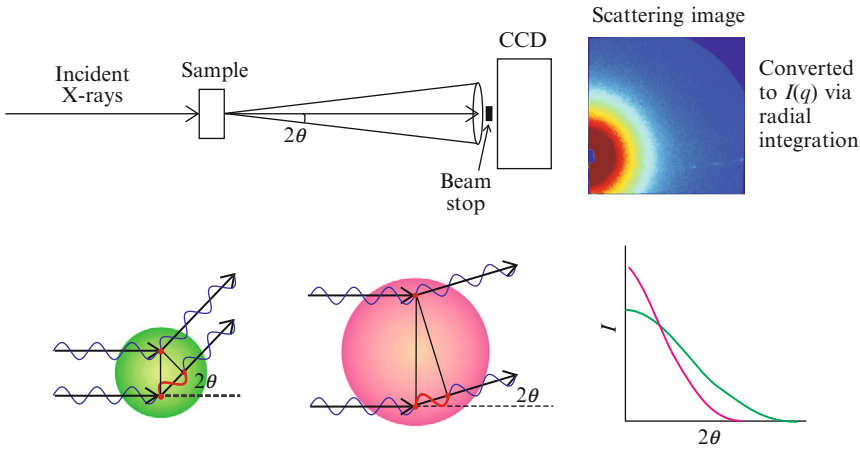

Figure 19.1 Schematic of a small angle X-ray scattering experiment. The top panel illustrates how a SAXS experiment is carried out. An X-ray beam, incident from the left, is scattered by the sample. The angular dependence of the scattered radiation is recorded on a two-dimensional CCD detector placed about 1 m downstream of the sample. A typical image from such a detector is shown at top, right. To avoid detector damage, the direct beam is blocked by a beam stop, which can be seen at the lower left of the image. The lower panel illustrates how the size of objects in the sample affects the scattering profiles. Scattering from smaller objects persists to higher angle than scattering from larger objects because the phase differences between scattered X-rays are smaller. For smaller objects destructive interference occurs at larger angles. In addition, the scattering in the forward direction (at zero angle) reflects the molecular weight of the sample. Thus, scattering from the larger (pink) object has a higher intensity at zero angle, but decreases more rapidly with angle than scattering from a smaller, less massive (green) object.

species of ion in an ion–DNA system. All elements possess a unique set of characteristic energies, corresponding to electron binding energies and can be individually targeted by tuning the energy of an X-ray beam until it exactly equals, or is resonant with a specific electronic transition. Near its resonant energy the scattering power of this element is reduced (e.g., Creagh, 1999). Thus, if scattering is measured far from a resonant edge and a second profile is measured close to a resonant edge, scattering from the resonant element will be altered. For these experiments, the contrast, or scattering strength of the ions alone has been modified. By precise subtraction of normalized signals, it is possible to obtain information about the spatial distribution of the resonant elements surrounding nonresonant structures. If ions with accessible resonant edges are employed, counterions around DNA can be targeted. This latter condition places severe restrictions on the elements that can be probed. Since most biologically interesting counterions (e.g., Na^+, K^+, Mg^{2+}, Ca^{2+}) are derived from low Z

(atomic number) elements, this lower bound is of interest. Due to experimental challenges associated with measurements at X-ray energies below about 6 keV, elements with Z greater than 24 (e.g., Mn) are most easily accessible.

2.3. Computation and interpretation of ASAXS signal

The amplitude of X-rays scattered into a particular direction (characterized by a momentum transfer $q = (4\pi/\lambda)\sin\theta$) is expressed as the product of a form factor, $F(q)$ that describes the shape of the "scatterer" and a scattering factor, f which reflects the electron density of the "scatterer" relative to the background. The latter factor is of critical importance to ASAXS. Far from the absorption edge, f has a constant value f_0, that of the X-ray atomic form factor that (in vacuum) is proportional to atomic number (Z); near the edge f changes dramatically. Due to "resonant scattering", the real part of f decreases by an amount denoted f', while an imaginary component, f'' appears at (and above) the edge, and accounts for absorption by the atom. Near an ion's absorption edge, the total scattering factor is energy dependent and expressed as

$$f_{\text{ion}} = f_0 + f'(E) + \mathrm{i}f''(E) \tag{19.1}$$

The energy dependent contributions to the scattering factor, f' and f'' are illustrated in Fig. 19.2 for cobalt. Cobalt is of interest to our work because of its presence within cobalt hexammine, a trivalent ion commonly used in nucleic acid studies.

For a multicomponent system consisting of ions plus DNA, the scattering amplitude is expressed as: $A_s = f_{\text{DNA}}F_{\text{DNA}}(q) + f_{\text{IONS}}F_{\text{IONS}}(q)$. Here, the f's represent the effective number of electrons that contribute to the scattering while the F's reflect the spatial arrangement of the scattering particles, thus $f_{\text{IONS}} = N_{\text{ions}}{}^{\star}f_{\text{ion}}$ where N_{ions} equals the number of ions associated to (condensed on) the nucleic acid. (Note that the effective number of electrons contributed to the scattering is computed relative to the solvent background. See Das *et al.* (2003b) for more information about this contrast.) Since detectors measure *intensity*, not amplitude, and the intensity $I(q)$ is the product of the scattering amplitude A_s and its complex conjugate $A_s^{\star}$:

$$I(q) = (f_{\text{DNA}}F_{\text{DNA}}(q) + f_{\text{IONS}}F_{\text{IONS}}(q))(f_{\text{DNA}}F_{\text{DNA}}(q) + f_{\text{IONS}}F_{\text{IONS}}(q))^{\star} \tag{19.2}$$

To compute $I(q, E)$ near the ion absorption edge (and far from any resonant edge for the DNA), the energy dependent expression for f_{ion} is substituted into the above equation. With the restriction that measurements are made *below* the edge, so $f''(E) \sim 0$, the intensity can be expressed as a quadratic function of $f'(E)$ (Patel *et al.*, 2004):

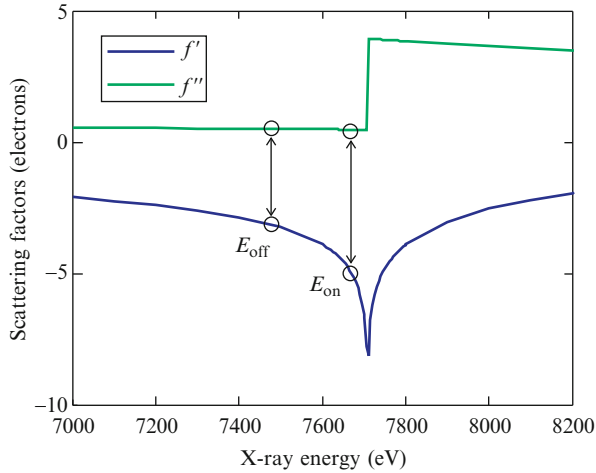

Figure 19.2 Changes in the scattering factor of cobalt near the cobalt absorption edge. At energies approaching the cobalt K-edge (7.71 keV), the effective scattering factor of cobalt changes due to anomalous or resonant effects. The lower curve reflects changes in the real part of the scattering factor, while the upper curve reflects changes in the imaginary part of the scattering factor (absorption). The circles represent typical working energies for an ASAXS experiment at this edge. Energies are selected to maximize changes in f' while keeping changes in f'' minimal.

$$I(q,E) = c + b \cdot f'(E) + a(f'(E)^2) \tag{19.3}$$

where

$$a = N_{\text{ions}}^2 F_{\text{IONS}}^2;\ b = N_{\text{ions}} \star (2 f_{\text{DNA}} F_{\text{DNA}} F_{\text{IONS}} + 2 f_0 N_{\text{ions}} F_{\text{IONS}}^2);$$
$$c = (f_{\text{DNA}} F_{\text{DNA}})^2 + 2 f_{\text{DNA}} f_0 N_{\text{ions}} F_{\text{DNA}} F_{\text{IONS}} + (f_0^2 N_{\text{ions}}^2 F_{\text{IONS}})^2$$

Thus, at each value of q, $I(q, E)$ varies with $f'(E)$ to the 0th, 1st, and 2nd order. The total number of electrons associated with the DNA is significantly larger than the total number of electrons associated with the counterion system, although the effects of hydration and electrostriction make it challenging to compute exact values for scattering factors *a priori* (Das *et al.*, 2003b). The third term in Eq. (19.3) is significantly smaller than the second, because the change in the contrast is typically a small fraction of the total contrast. Thus, if measurements are carried out at only two energies below the edge, the intensity difference is well approximated by linear variation:

$$\Delta I(q) = b \cdot (f'(E_2) - f'(E_1)) \sim F_{\text{DNA}} F_{\text{IONS}} \tag{19.4}$$

This approximation assumes that contributions from the F_{IONS}^2 term are smaller than those resulting from the $F_{\text{DNA}} F_{\text{ion}}$ terms because in general $f_{\text{DNA}} F_{\text{DNA}}$ is larger than $f_0 N_{\text{ions}} F_{\text{IONS}}$.

Three products of form factors occur in Eq. (19.3): $F_{\mathrm{DNA}}F_{\mathrm{DNA}}$, $F_{\mathrm{DNA}}F_{\mathrm{IONS}}$, and $F_{\mathrm{IONS}}F_{\mathrm{IONS}}$. Figure 19.3 provides guidance for interpreting each of these terms. The interference term of Eq. (19.4) depends on both the structure of the DNA and the spatial distribution of the counterion cloud surrounding it. In simple terms, it reflects the set of all vectors that have one end inside the DNA and the other end in the ion cloud (such as the red arrow in Fig. 19.3). In this chapter, we report on anomalous signals derived from the difference between scattering intensities taken at two energies (Eq. (19.4)). Extraction of all three terms in Eq. (19.3) requires precise measurement of the (smaller) F^2_{IONS} term. As discussed in the literature (Jusufi and Ballauff, 2006), we note that the "*a*" term can be extracted from a quadratic fit, if measurements are carried out at several energies such that $f'(E)^2$ varies by an order of magnitude. The coefficient of this term, F^2_{IONS} directly reports the spatial distributions of the ions without reference to the structure of the DNA. Efforts are currently underway to measure this term for ions around DNA.

In summary, ASAXS has the potential to provide information both about the association of counterions to a *macroion*, as well as about the

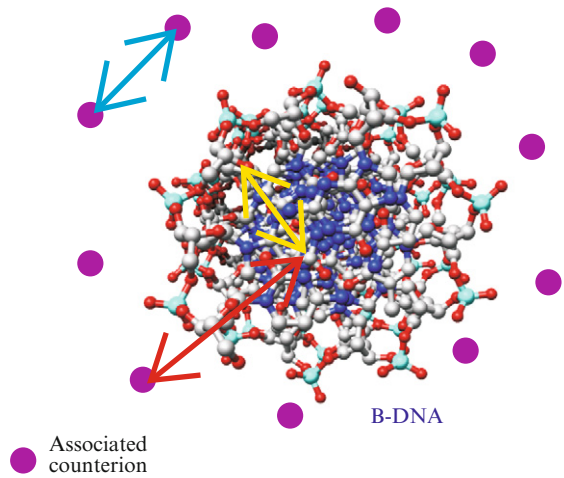

Figure 19.3 Interpretation of form factor products in Eq. (19.3). This figure illustrates the meaning of the cross-terms of Eq. (19.3), using an atomic representation of B-DNA, along with condensed counterions (blue circles). The $F_{\mathrm{DNA}}F_{\mathrm{DNA}}$ term, discussed in the text, is related to the set of all vectors that begin and end in the DNA, for example, the yellow arrow. The $F_{\mathrm{DNA}}F_{\mathrm{IONS}}$ term is related to the set of all vectors with one end in the DNA and the other end in the counterion cloud, for example, the red arrow. Finally, the $F_{\mathrm{IONS}}F_{\mathrm{IONS}}$ term is related to the set of all vectors connecting ions, represented by the cyan arrow in the figure.

structure of the ion cloud alone. Analysis and interpretation of the data is discussed in a later section.

3. Experimental Setup: Samples

3.1. Sample preparation

Samples discussed here are annealed duplexes of single-stranded 25 nucleotide desalted and purified DNA (IDT, Coralville, IA) and RNA molecules (Lafayette, CO) (Andresen *et al.*, 2004, 2008; Das *et al.*, 2003b; Pabit *et al.*, 2009). The duplex strands were dialyzed extensively to a specific bulk salt concentration (e.g., 100 m*M* $Rb(CH_3COO)$ and 0.5 m*M* $Co(NH_3)_6Cl_3$) and buffer solutions using microcon centrifugal filter units (Millipore Corporation, Billerica, MA). This dialysis step is important because it ensures that the condensed ions around the nucleic acids and ions in the bulk solution were able to attain equilibrium. Note that we favor the lower molecular weight anion acetate, as opposed to Cl^- to minimize background scattering. After dialysis, the nucleic acid solutions are brought to a final volume of 40 μl and final duplex concentrations of 0.2–0.6 m*M*.

4. Experimental Setup: Beamline

4.1. From source to sample

The following information is based on experience using a single beamline (CHESS C-line), over approximately 5 years. A bend magnet source of synchrotron radiation X-rays has proved quite adequate for a wide range of ASAXS measurements. The beamline delivers flux at the sample of up to 5×10^{11} photons/s/mm^2, in bandwidth $\Delta E/E \sim 0.00025$ at 10 keV, using a silicon (220) double crystal monochromator (mono). The mono is set to collect up to two horizontal milliradians that is focused (approximate ratio 3:1) at a convenient point between the sample and detector. This point is determined by the maximum horizontal sample size. One can reduce horizontal divergence at the cost of intensity. Before a recent upgrade, a flat rhodium coated, postmono mirror was used in conjunction with monocrystal detuning to suppress high-energy harmonics. The upgrade provides vertical focusing capability upstream of the mono, increasing flux by two to three times, without appreciable change in divergence. The effect of the horizontal divergence is to "blur" the scattering pattern in this direction. Although the blurring is pronounced only along the horizontal direction, we accept scattering data that fall within $\pm 45^\circ$ around the vertical. The width of a peak in the scattering profile from our polycrystalline calibrant

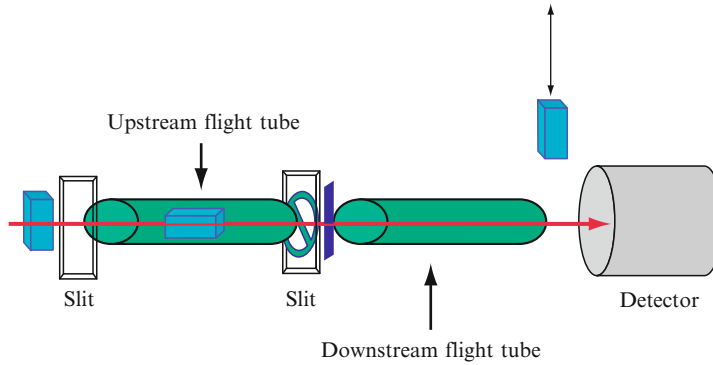

Figure 19.4 A schematic view of the ASAXS setup; downstream is to the right. Ion chambers (blue) monitor beam intensity before and after the main slit, and can be inserted for measurement of sample transmittance between downstream flightpath (green) and CCD X-ray detector. A guard slit with built-in shutter and sample is located between the flight tubes. All slits are moved under user control. The flight tube upstream of the sample is helium filled and contains a built-in ion chamber; the downstream path is vacuum terminated by silicon nitride at the front end and Kapton at the detector end. A beamstop with transverse position control is located in the vacuum; it is made from amorphous metal that greatly reduces energy dependent powder diffraction structures that can compromise the beamstop scattering used to monitor beam transmission through the sample.

silver stearate displays no broadening on this scale. A schematic drawing of the ASAXS beamline is shown in Fig. 19.4.

4.2. Sample cells

Small volume ($\sim$30 μl) sample cells are manufactured by machining a rectangular hole through a flat piece of acrylic. The X-ray energy (determined by the resonant energy for ASAXS experiments) dictates the acrylic (and sample) thickness. Thin cells are better suited for lower energies due to increased absorption. For measurements near 8 keV (Co K-edge) $\sim$1 mm is optimal while $\sim$3 mm sample thickness is used at 15–16 keV (Rb and Sr K-edges). The cells are fitted with silicon nitride windows, fabricated at the Cornell Nanoscale Science and Technology Facility using a wet-etch process. Ultrathin windows provide good signal-to-noise by minimizing background absorption and scattering and allowing accurate background subtraction (Andresen *et al.*, 2004). Window fabrication is discussed in more detail in Chapter 12. Small holes are drilled through the acrylic into the sample volume to enable filling by syringe. Figure 19.5 shows a photograph of the sample cells, with details provided in the caption.

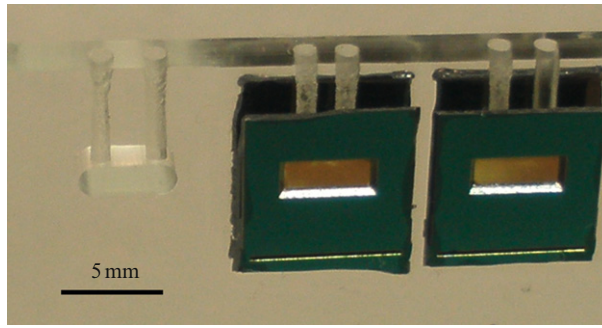

Figure 19.5 The ASAXS sample cells. This photograph shows three adjacent sample cells used for ASAXS measurements. As described in the text, the cells are machined from acrylic. The long fill holes that run up and down are used to load and unload the cells. The leftmost cell in the photograph is unsealed; the two cells at the right have been sealed with silicon nitride windows. The silicon nitride free standing membrane is the light green rectangle at the center of the silicon supporting frame.

4.3. From sample to detector

After passing though the sample cell, the scattered X-rays travel to the detector through an evacuated flight tube. The use of vacuum eliminates additional background arising from air scatter. Near the end of the flight tube, a motorized (XIA, Hayward, CA) beam stop prevents the direct beam from reaching the CCD detector (homebuilt 1 K, fiber-optically bonded CCD; Tate *et al.*, 1995) used in collecting the scattering data. Compton scattering from the beam stop passes though a vacuum-sealed Kapton window on one side of the flight tube to an Xflash detector (Rontec, Carlisle, MA) which monitors the X-ray intensity transmitted through the sample cell and allows intensity normalization of the data. The distance between the sample cell and the CCD is about 1 m.

5. Data Acquisition

For anomalous scattering experiments, data are acquired near the K absorption edge energies of chosen elements. The energy constraints, discussed above, require that we study monovalent Rb^{+} (edge at 15.2 keV), divalent Sr^{2+} (16.1 keV), and trivalent cobalt hexammine (Co edge at 7.71 keV) to monitor ion distributions around DNA. The energy resolution of the beamline monochromator varies from 2 to 4 eV between 7.5 and 16.1 keV. To obtain the anomalous signal, $\Delta I(q)$, Eq. (19.4), we acquire

scattering data at two X-ray energies. The first is well below ($E_{\text{off-edge}}$ or E_{off}), and the second near ($E_{\text{on-edge}}$ or E_{on}) the absorption edge. From Eqs. (19.3) and (19.4), we show that the difference of E_{on} and E_{off} scattering profiles removes the energy independent terms and yields the anomalous scattering signal Eq. (19.4), written explicitly as

$$\Delta I(q) = I(q, E_{\text{off}}) - I(q, E_{\text{on}}) \approx 2 f_{\text{DNA}} F_{\text{DNA}}(q) N_{\text{ions}} (f'(E_{\text{off}}) - f'(E_{\text{on}})) F_{\text{IONS}} \tag{19.5}$$

Energies are selected from transmission scans of a reference solution containing the ion of interest. Care must be taken to find the X-ray edge, which may be shifted from the edge of a pure metal reference. The on energy is set to maximize the magnitude of $\Delta f'(E)$ while $\Delta f''(E)$ and fluorescence contributions to the image are very small (see Fig. 19.2). To illustrate how X-ray energies, E_{on} and E_{off}, are determined, consider measurements near the Rb edge. From measurements of the energy-dependent transmission through a Rb–Acetate solution the absorption peak was determined to be 15.230 keV. We set the "on" energy just below the onset of absorption, $E_{\text{on}} = 15.213$ keV, while $E_{\text{off}} = 15.113$ keV is well below the absorption edge.

To minimize time-dependent systematic errors, data are collected using the following acquisition sequence: two images at E_{off}, four images at E_{on}, two images at E_{off}. We repeat this sequence either eight (or 16) times. For effective background subtraction, anomalous scattering data acquisition of the sample is bracketed by four (or eight) sequences of buffer images, taken immediately before and after the DNA measurements. Buffer background images are acquired by measuring SAXS profiles of solutions used for dialysis. This procedure yields a total of 32 (or 64) E_{off} images and 32 (or 64) E_{on} images per sample. At higher (i.e., Rb and Sr) energies where there is reduction in background scattering, 32 images per energy per sample suffice to achieve good signal to noise ratio. For the lower energy Co experiments, 64 images per energy per sample are required. The X-ray exposure time per image is 10 s, and the total exposure is below the threshold for radiation damage at CHESS C-line. Images are radially integrated to produce a one-dimensional I versus q curve. Decay of X-ray beam intensity over time, as well as any energy dependent differences in transmission are accounted for by transmitted beam intensity normalization.

Figure 19.6 illustrates how we process the two-energy data and generate the ASAXS profiles. First, we average the set of all DNA and buffer intensity profiles at each of the two energies. The averaged data are displayed in Fig. 19.6A. Note that both DNA and buffer profiles, taken at E_{on}, have slightly elevated background relative to E_{off} data; this is due to X-ray fluorescence. Most of this fluorescence background is removed by buffer subtraction (see Fig. 19.6B). The remaining on-edge fluorescence results

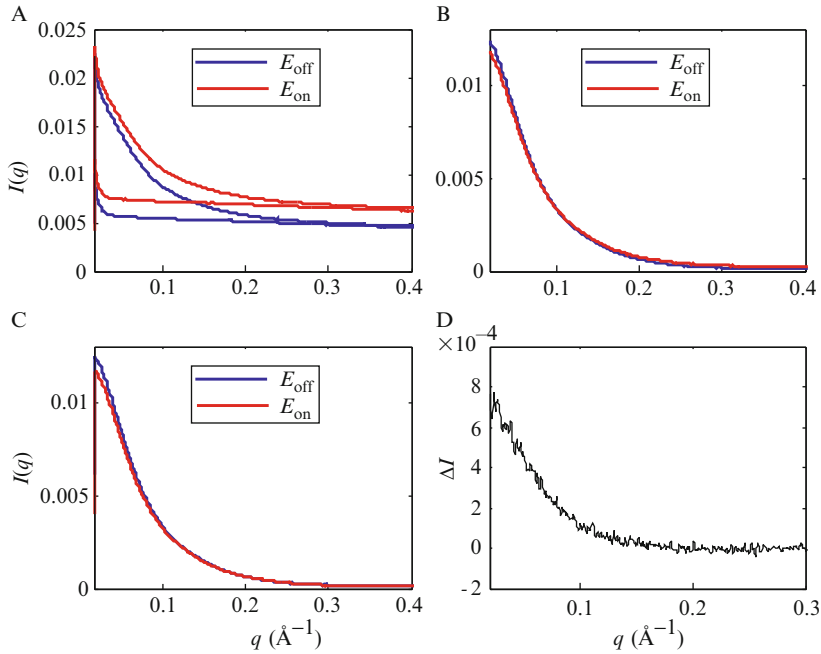

Figure 19.6 Demonstration of data processing to generate ASAXS profiles. Panel (A) shows the raw data, acquired at the two ASAXS energies, along with the corresponding buffers. Panel (B) shows the buffer subtracted curves at each energy. Panel (C) shows the data after corrections have been applied to account for energy dependent effects and for fluorescence, detailed in the text. Panel (D) illustrates the measured difference signal: $I(E_{off}) - I(E_{on})$.

from the slightly elevated concentration of ions in the DNA-containing solution compared to the buffer solution. We compute the additive correction resulting from this offset, $\text{fluor}_{\text{offset}}$, by matching E_{on} and E_{off} profiles at high q. It is also critically important to account for the changing transmission of all beamline components as the energy is varied, as well as the energy response of all detectors. A multiplicative correction factor $\lambda_{\text{correction}}$ is computed, based on differences between on- and off-edge profiles of DNA in nonresonant buffers of identical ionic strength. The correction factor $\lambda_{\text{correction}} = I_{\text{nonrsnt}}(q, E_{\text{off}})/I_{\text{nonrsnt}}(q, E_{\text{on}})$ is typically computed from a sample dialyzed against for example, 100 m*M* NaCl instead of 100 m*M* Rb–Acetate. Here, I_{nonrsnt} is the scatting from the nonresonant sample. Typically, this multiplicative factor is equal or very close to unity. The corrected SAXS signals are represented by Eq. (19.6) and shown in Fig. 19.6C.

$$I_{\text{corr}}(q, E_{\text{on}}) = I(q, E_{\text{on}}) \cdot \lambda_{\text{correction}} - \text{flour}_{\text{offset}}$$
$$I_{\text{anom}}(q) = I(q, E_{\text{off}}) - I_{\text{corr}}(q, E_{\text{on}}) \quad (19.6)$$

The corresponding ASAXS profiles, $I_{\text{anom}}(q)$, are shown in Fig. 19.6D. Note that the difference signal is small. This signal arises from approximately 40 Rb^+ ions per 25 bp DNA and typically is one order of magnitude smaller than the on- or off-energy SAXS profiles. However, these ASAXS data collection methods produce results that are robust and reproducible between runs.

6. Results and Data Analysis

ASAXS provides valuable spatial information about ions associated to nucleic acids. Because ion resonance is X-ray energy specific, a particular ionic species can be targeted in ASAXS experiments (even in conditions where there are multiple ionic species in the bulk solution). In this section, we provide several examples of how ASAXS experiments can be used to study counterion atmospheres around DNA and RNA.

6.1. Comparison of spatial distributions for ions of different valence

The shape and extent of the anomalous signal can used to probe the spatial distribution of selected valence ions around DNA. In Fig. 19.7, we show the increase in high-angle (high q) anomalous scattering as the ion valence increases from 1 to 3. Note that X-ray scattering from a larger object falls off more rapidly than scattering from a smaller object (illustrated in Fig. 19.1). In ASAXS, the anomalous signals generally represent the set of all vectors with one end inside DNA and the other in the ion cloud. Thus, ASAXS signals persisting to higher q represent shorter vectors linking DNA to ions. Through this qualitative comparison, we find that higher valence ions are more tightly bound (more localized) to the DNA surface than lower valence ions (Andresen *et al.*, 2004, 2008).

6.2. ASAXS probes competition of different ionic species

When a solution contains multiple ionic species, ASAXS can be used to determine the fractional contribution of each cationic species to the ion atmosphere around nucleic acids. As an illustration, we show monovalent and trivalent ion competition around DNA. Figure 19.8A displays anomalous difference signal from Rb^+ ions bound to DNA in two solutions. In a

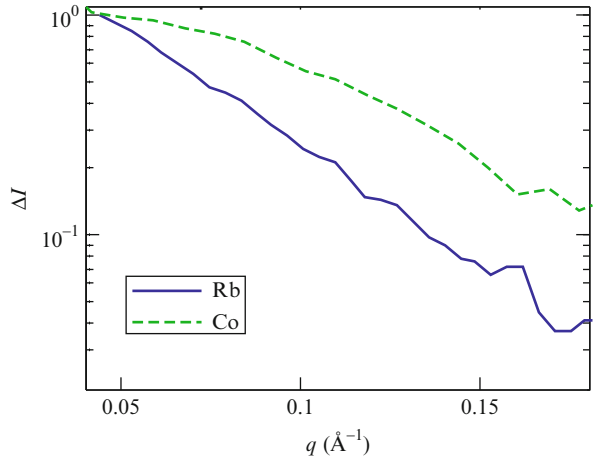

Figure 19.7 Monovalent and trivalent ASAXS signal comparison. This figure illustrates differences in shape between the ASAXS signals for monovalent Rb around DNA and trivalent cobalt hexammine around DNA. The curves have been scaled to match at the lowest q to enable shape comparison. The increase in high-angle scatter associated with the trivalent relative to monovalent ion signal, suggests that the trivalent ions are more tightly localized to the DNA.

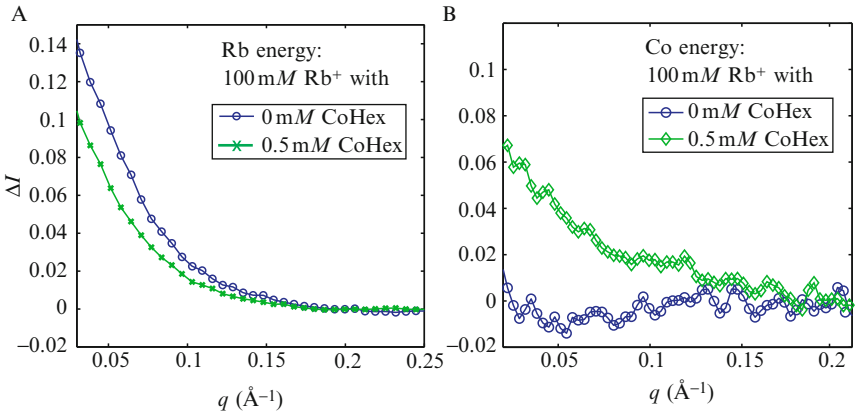

Figure 19.8 Anomalous signals of DNA in 100 mM Rb^+ (blue curves) and in a solution containing both 0.5 mM $[Co(NH_3)_6]^{3+}$ and 100 mM Rb^+ (green curves). Panel (A) shows the ASAXS signal acquired at the Rb energy for both of these samples. In the pure Rb sample (blue), all of the condensed counterions are Rb^+. The Rb anomalous signal drops after even small amounts of cobalt hexammine are added, reflecting the very efficient replacement of monovalent by trivalent ions. The bulk Rb ion concentration is identical for both samples: the anomalous signal reports on the condensed counterions. Panel (B) shows ASAXS curves acquired on the same samples at the Co energy. In the pure Rb sample (blue curve), no cobalt hexammine is present and the signal intensity is zero. The green curve shows the increasing cobalt anomalous signal, reflecting the presence of cobalt in the counterion cloud.

solution containing DNA in 100 m*M* Rb^+ ions, there is a large anomalous signal; yet when even small amounts of trivalent ions are added to the solution (0.5 m*M* $[Co(NH_3)_6]^{3+}$ ion), the monovalent ions are rapidly displaced from around DNA and the Rb anomalous signal decreases significantly. Although the bulk concentration of Rb^+ is equal for both experiments, the decrease in bound Rb^+ occurs because of strong competition from trivalent $[Co(NH_3)_6]^{3+}$. The corresponding increase in the Co anomalous signal is shown in Fig. 19.8B. The change in amplitude of the ASAXS signal is quantified by integrating the total anomalous scattering profile and scaling this signal to reflect the DNA charge. Within the approximations discussed herein, this yields the relative number of ions around the DNA. This value was further verified by comparing the integrated magnitude of the ASAXS signal with results from ICP experiments on identically prepared samples. The latter measurements report the number of excess cations, and are in good agreement with the ASAXS results. Figure 19.9 shows the integral of the ASAXS signals at the Rb and Co energies and the comparison to the predictions to the nonlinear Poisson–Boltzmann (NLPB) equation, using the APBS package for comparison (Baker *et al.*, 2001). Note the marked decrease in the number of bound Rb^+ ions as the concentration of the competing trivalent ion is increased while the bulk monovalent ion concentration is kept at 100 m*M*. Details of this experiment can be found in Andresen *et al.* (2008).

6.3. Comparing experimental ASAXS profiles with NLPB simulations

While most previous ASAXS studies have focused on DNA, we have recently used ASAXS to probe the counterion distribution around double-stranded RNA molecules. In previous work, we showed that numerical calculations using an ion-size corrected NLPB model adequately describes ASAXS data (Andresen *et al.*, 2004; Das *et al.*, 2003a,b). By comparing experimental ASAXS profiles with simulations based on the NLPB equation (Pabit *et al.*, 2009), we found that the RNA anomalous signal is more sensitive to the choice of probe ion radius used in the calculations (see Fig. 19.10). In fact, an ion radius upper bound of 4 Å is necessary to adequately describe RNA ASAXS data. In the case of DNA, a wider range of 2–6 Å ion radii sufficiently describes the data (see Fig. 19.9). We attribute the difference between DNA and RNA to A-form helix topology. The RNA A-form helix has a deeper and narrower major groove compared to the DNA B-form helix. We find that counterions penetrate the A-form major groove as suggested by past crystallographic (Robinson *et al.*, 2000) and theoretical (Chin *et al.*, 1999; Mills *et al.*, 1992) studies. In general, the counterions are more closely localized to the RNA central axis than DNA as shown in the ASAXS profiles displayed in Fig. 19.11A. RNA anomalous

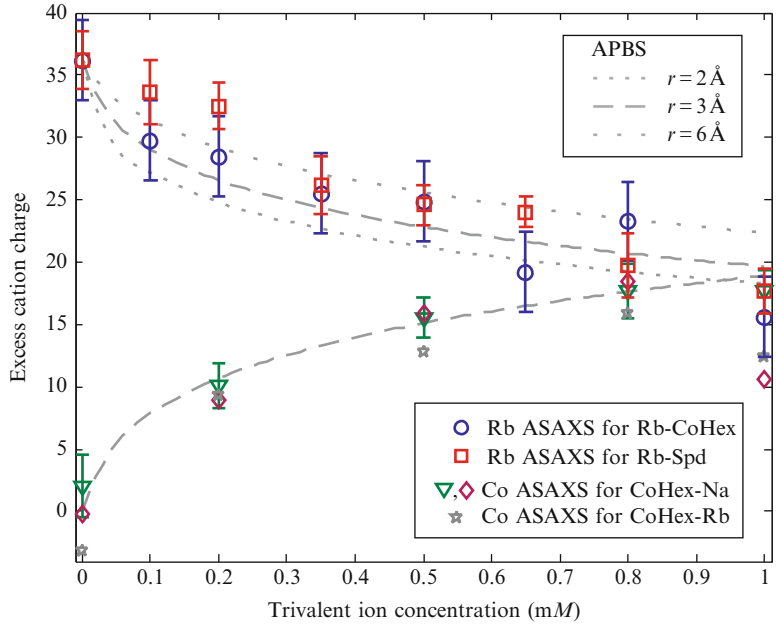

Figure 19.9 Comparison of counterion competition data with the numerical solution of the PB equation from APBS. Upper half: DNA charge compensated by Rb^+ ions in competition with $(Co(NH_3)_6)^{3+}$ (*circles*) and spermidine^{3+} (*squares*) in 100 m*M* RbCl, 0.2 m*M* [DNA]. Lower half: DNA charge compensated by $(Co(NH_3)_6)^{3+}$ ions in competition with 100 m*M* NaCl at 0.2 m*M* [DNA] (*triangles*) and in competition with 100 m*M* NaCl (*diamonds*) or RbCl (*stars*) at 0.6 m*M* [DNA]. Data without error bars have errors smaller than symbol size. The dashed lines represent APBS computations for DNA surrounded by ions with different radii. A 2 Å ion radius underestimates the fraction of monovalent ions in the atmosphere. The data are consistent with ion radii of 3 Å or greater with an upper bound of 6 Å. (Figure and caption reproduced with permission from Andresen *et al.* (2008).)

signals persist at higher q suggesting closer association of counterions to the RNA molecules.

Another comparison of experimental and theoretical data is shown in Fig. 19.11B and C. Here, we compute the radial Patterson inversions, $U(R)$, of the experimental data (Fig. 19.11B) for comparison with the simulations (Fig. 19.11C).

The radial Patterson inversion of the anomalous difference signal is calculated using

$$U(R) = \frac{R}{4\pi^2}\int q \cdot I_{\text{anom}}(q) \cdot \sin(qR)\, \mathrm{d}q \tag{19.7}$$

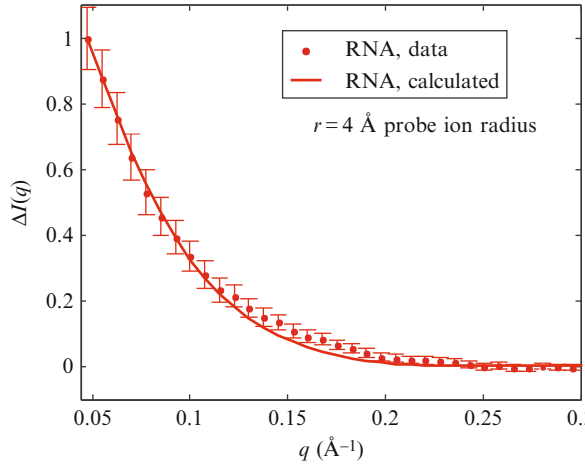

Figure 19.10 RNA ASAXS data compared with APBS predictions. This figure shows the measured anomalous difference signal for Rb-RNA in comparison with predictions generated using APBS. To obtain good agreement, the finite size of the ion must be included. In this case, an ion probe radius of 3 or 4 Å (pictured) optimizes the comparison.

as described by Engelman *et al.* (1975). In the ideal case, $U(R)$ reports on the distribution of vector lengths correlating nucleic acids with the condensed counterions, supporting our qualitative result that ions are more closely localized to the RNA than the DNA. However, some caution must be employed when using Patterson inversions in describing ASAXS data because the anomalous signal contains small contributions from ion–ion distances, as shown in Eqs. (19.3) and (19.4). We note that ion–ion distances should mimic the DNA– or RNA–ion distances since ions that are tightly bound to the nucleic acid are also closely associated with each other. Due to the complexities in separating out the different terms illustrated in Fig. 19.3, it is most straightforward to analyze and interpret the data by direct comparison to simulations.

7. Conclusion

Overall, this chapter shows how ASAXS data can be acquired and carefully interpreted to yield information related to the spatial distribution and number of counterions associated to DNA. Due to the small size of the signal, ASAXS requires careful attention to experimental detail. Background scattering must be minimized to the greatest possible extent.

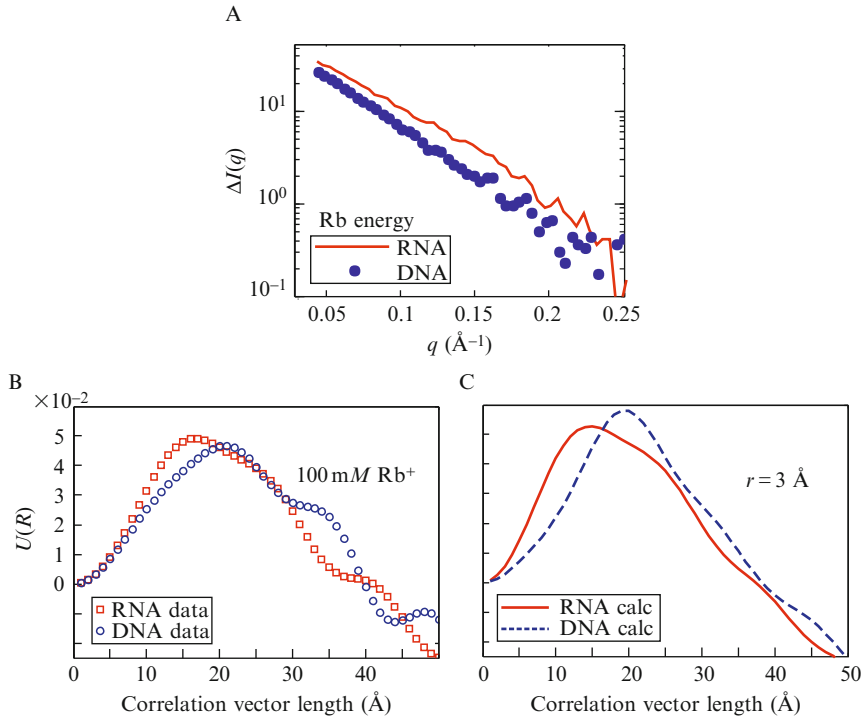

Figure 19.11 Comparison of anomalous signals obtained for Rb-RNA and Rb-DNA. Panel (A) shows the ASAXS signals for both DNA and RNA displayed on a log scale. Panels (B) and (C) illustrate an alternative method for comparing measured with predicted ion distributions. A radial Patterson inversion can be applied both to the data and to the curve generated from simulation. Although it is challenging to interpret this curve directly (see text), it is instructive to compare experiment with prediction in this form. When an ion probe radius of 3 Å is used, the differences in ion distribution between RNA and DNA are clearly mirrored by simulation.

The most robust analysis methods involve direct comparison of the $\Delta I(q)$ term with theoretical computations. Agreement between data and prediction then validate the models used. The application of "inversion" approaches involves taking Fourier transforms of the data to yield the set of vectors connecting scattering particles. However, one must be cautious when interpreting the results of these inversions. Experiments are currently underway to measure the F^2_{IONS} term independently, which will allow us to extract the pure ion–DNA cross-term which is more straightforward to interpret.

In spite of challenges, ASAXS continues to provide unique information about ions associated to DNA or RNA.

ACKNOWLEDGMENTS

We acknowledge those who have contributed to the ASAXS projects: K. Andresen, R. Das, S. Doniach, D. Herschlag, L. Kwok, J. Lamb, L. Li, G. Maskel, S. Meisburger, T. Mills, H. Y. Park, and X. Qiu. Funding for this work was provided by NSF through grant MCB-0347220, and by the NIH through P01-GM066275. CHESS is supported by the NSF and the NIH/NIGMS under Grant No. DMR-9713424. The CNF is supported by the NSF, Cornell University and industrial affiliates.

REFERENCES

Anderson, C. F., and Record, M. T. (1990). Ion distributions around DNA and other cylindrical polyions—Theoretical descriptions and physical implications. *Annu. Rev. Biophys. Biophys. Chem.* **19,** 423–465.

Andresen, K., Das, R., Park, H. Y., Smith, H., Kwok, L. W., Lamb, J. S., Kirkland, E. J., Herschlag, D., Finkelstein, K. D., and Pollack, L. (2004). Spatial distribution of competing ions around DNA in solution. *Phys. Rev. Lett.* **93,** 248103.

Andresen, K., Qiu, X., Pabit, S. S., Lamb, J. S., Park, H. Y., Kwok, L. W., and Pollack, L. (2008). Mono and tri-valent ions around DNA: A small angle scattering study of competition and interactions. *Biophys. J.* **95,** 287–295.

Bai, Y., Greenfeld, M., Travers, K. J., Chu, V. B., Lipfert, J., Doniach, S., and Herschlag, D. (2007). Quantitative and comprehensive decomposition of the ion atmosphere around nucleic acids. *J. Am. Chem. Soc.* **129,** 14981–14988.

Baker, N. A., Sept, D., Joseph, S., Holst, M. J., and McCammon, J. A. (2001). Electrostatics of nanosystems: Application to microtubules and the ribosome. *Proc. Natl. Acad. Sci. USA* **98,** 10037–10041.

Bloomfield, V. A., Crothers, D. M., and Tinoco, I. J. (2000). Nucleic acids: Structures, properties and functions. University Science Books, Sausalito, CA.

Chin, K., Sharp, K. A., Honig, B., and Pyle, A. M. (1999). Calculating the electrostatic properties of RNA provides new insights into molecular interactions and function. *Nat. Struct. Biol.* **6,** 1055–1061.

Creagh, D. C. (1999). X-ray dispersion corrections. The International Union of Crystallography, Dordrecht/Boston/London.

Das, R., Kwok, L. W., Millett, I. S., Bai, Y., Mills, T. T., Jacob, J., Maskel, G. S., Seifert, S., Mochrie, S. G. J., Thiyagarajan, P., Doniach, S., Pollack, L., *et al.* (2003a). The fastest global events in RNA folding: Electrostatic relaxation and tertiary collapse of the tetrahymena ribozyme. *J. Mol. Biol.* **332,** 311–319.

Das, R., Mills, T. T., Kwok, L. W., Maskel, G. S., Millett, I. S., Doniach, S., Finkelstein, K. D., Herschlag, D., and Pollack, L. (2003b). The counterion distribution around DNA probed by solution X-ray scattering. *Phys. Rev. Lett.* **90,** 188103.

Doniach, S. (2001). Changes in biomolecular conformation seen by small angle X-ray scattering. *Chem. Rev.* **101,** 1763–1778.

Engelman, D. M., Moore, P. B., and Schoenborn, B. P. (1975). Neutron-scattering measurements of separation and shape of proteins in 30s ribosomal-subunit of *Escherichia coli*—S2–S5, S5–S8, S3–S7. *Proc. Natl Acad. Sci. USA* **72,** 3888–3892.

Glatter, O. (1982). Small Angle X-Ray Scattering. Academic Press, New York.

Grilley, D., Soto, A. M., and Draper, D. E. (2009). Direct quantitation of Mg(2+)-RNA interactions by use of a fluorescent dye. *Methods Enzymol.* **455,** 71–94.

Jusufi, A., and Ballauff, M. (2006). Correlations and fluctuations of charged colloids as determined by anomalous small-angle X-ray scattering. *Macromol. Theory Simul.* **15,** 193–197.

Manning, G. S. (1969). Limiting laws and counterion condensation in polyelectrolyte solutions. 2. Self-diffusion of small ions. *J. Chem. Phys.* **51,** 934–938.

Mills, P. A., Rashid, A., and James, T. L. (1992). Monte-Carlo calculations of ion distributions surrounding the oligonucleotide D(Atatatatat)2 in the B-conformations, a-conformations, and wrinkled D-conformations. *Biopolymers* **32,** 1491–1501.

Pabit, S. A., Qiu, X. Y., Lamb, J. S., Li, L., Meisburger, S. P., and Pollack, L. (2009). Both helix topology and counterion distribution contribute to the more effective charge screening in dsRNA compared with dsDNA. *Nucleic Acids Res.* **37,** 3887–3896.

Patel, M., Rosenfeldt, S., Ballauff, M., Dingenouts, N., Pontoni, D., and Narayanan, T. (2004). Analysis of the correlation of counterions to rod-like macroions by anomalous small-angle X-ray scattering. *Phys. Chem. Chem. Phys.* **6,** 2962–2967.

Plum, G. E., and Bloomfield, V. A. (1988). Equilibrium dialysis study of binding of hexammine cobalt(III) to DNA. *Biopolymers* **27,** 1045–1051.

Robinson, H., Gao, Y. G., Sanishvili, R., Joachimiak, A., and Wang, A. H. J. (2000). Hexahydrated magnesium ions bind in the deep major groove and at the outer mouth of A-form nucleic acid duplexes. *Nucleic Acids Res.* **28,** 1760–1766.

Stuhrmann, H. B. (1981). Anomalous small-angle scattering. *Q. Rev. Biophys.* **14,** 433–462.

Svergun, D. I., and Koch, M. H. J. (2003). Small-angle scattering studies of biological macromolecules in solution. *Rep. Prog. Phys.* **66,** 1735–1782.

Tate, M. W., Eikenberry, E. F., Barna, S. L., Wall, M. E., Lowrance, J. L., and Gruner, S. M. (1995). A large-format high-resolution area X-ray-detector based on a fiberoptically bonded charge-coupled-device (CCD). *J. Appl. Crystallogr.* **28,** 196–205.

Wensel, T. G., Meares, C. F., Vlachy, V., and Matthew, J. B. (1986). Distribution of ions around DNA, probed by energy-transfer. *Proc. Natl Acad. Sci. USA* **83,** 3267–3271.